Theory for the anomalous electron transport in Hall effect thrusters. I. Insights from particle-in-cell simulations

T. Lafleur,[1,2,a)] S. D. Baalrud,[3] and P. Chabert[1]

[1]*Laboratoire de Physique des Plasmas, CNRS, Sorbonne Universités, UPMC Univ Paris 06, Univ Paris-Sud, Ecole Polytechnique, 91128 Palaiseau, France*
[2]*Centre National d'Etudes Spatiales (CNES), F-31401 Toulouse, France*
[3]*Department of Physics and Astronomy, University of Iowa, Iowa City, Iowa 52242, USA*

Using a 1D particle-in-cell simulation with perpendicular electric, E_0, and magnetic, B_0, fields, and modelling the azimuthal direction (i.e., the $E_0 \times B_0$ direction), we study the cross-field electron transport in Hall effect thrusters (HETs). For low plasma densities, the electron transport is found to be well described by classical electron-neutral collision theory, but at sufficiently high densities (representative of typical HETs), a strong instability is observed to significantly enhance the electron mobility, even in the absence of electron-neutral collisions. This instability is associated with correlated high-frequency (of the order of MHz) and short-wavelength (of the order of mm) fluctuations in both the electric field and the plasma density, which are shown to be the cause of the anomalous transport. Saturation of the instability is observed to occur due to a combination of ion-wave trapping in the $E_0 \times B_0$ direction, and convection in the E_0 direction. *Published by AIP Publishing.*
[http://dx.doi.org/10.1063/1.4948495]

I. INTRODUCTION

Hall effect thrusters (HETs) are an important plasma technology that have been successfully used for almost 50 years as primary or secondary propulsion systems for a range of different spacecraft missions.[1–3] Typical HETs consist of an annular ceramic channel that is terminated at one end by an anode (through which propellant gas is injected) and open at the opposite end. A hollow cathode is located external to the channel and is used as an electron source to both sustain the plasma discharge and provide electrons to neutralize the accelerated ion beam. A large potential difference (hundreds of volts) is applied between the anode and the hollow cathode, which accelerates ions downstream to generate thrust, while accelerating some electrons upstream towards the anode. These electrons are strongly impeded by an external, and predominantly radial, magnetic field created with permanent magnets or solenoids and a specially designed magnetic circuit. This magnetic field increases the electron residence time, hence promoting efficient ionization and ensuring that essentially all of the input propellant gas is ionized.[3]

Despite the critical role that suppressed cross field electron transport plays in the HET operation, numerous studies have shown that the electron mobility across the magnetic field is anomalously high and cannot be explained by classical diffusion theories based on standard electron-neutral or electron-ion collisions.[1,3–5] Even more disconcerting is the fact that the anomalous electron mobility appears to be highest in the near-field region just downstream of the thruster exit,[4–7] a region which would otherwise be expected to be very quiescent. Over the years, extensive experimental, theoretical, and numerical works have been undertaken to understand and explain these anomalies. A number of different

mechanisms have been proposed, including: (1) enhanced electron conductivity near the inner channel walls due to intense secondary electron emission arising from electron-wall collisions,[1,8,9] (2) the formation of strong instabilities due to the large electron drift velocities in the azimuthal direction,[10–13] (3) sheath instabilities[9,14] in the radial direction due to secondary electron emission, and (4) gradient-driven fluid instabilities.[15–17] While there is experimental confirmation that the thruster wall materials play a role in the electron transport,[3,8,9,18] there is mounting evidence suggesting electron-wall collisions and secondary electron emission are not sufficient to explain the observed cross-field transport.[10,19–23]

It thus seems that the most likely explanation for the anomalous transport is related to the formation of instabilities in the azimuthal direction, which have been directly observed in a number of experimental and numerical studies.[24–28] Such instabilities are driven by the large electron drift velocities in this direction,[11,12,29] which are often as fast as the electron thermal velocity itself, and which lead to large amplitude fluctuations in both the azimuthal electric field and the plasma density. The importance of these instabilities was emphasised in the 2D particle-in-cell (PIC) simulations of Ref. 11, which modelled the axial-azimuthal direction of an HET. With no adjustable parameter (which is usually needed in all fluid and axial-radial PIC simulations[20,30–36]), these simulations were able to reproduce a number of important experimental observations, including the demonstration of an enhanced electron cross-field mobility.[5] In addition, these simulations did not explicitly model the radial thruster walls, or secondary electron emission, suggesting that any enhancement of the electron transport by these factors is only an auxiliary effect. The instabilities in these simulations had frequencies in the MHz range,

a)Electronic mail: trevor.lafleur@lpp.polytechnique.fr

    23, 053502-1

wavelengths of the order of mm, and electric field amplitudes almost as large as the axial accelerating field due to the applied potential itself.[5] Some of the results in these original simulations have been independently confirmed by similar 2D simulations in Ref. 37.

These previous results suggest that kinetic instabilities driven by the azimuthal electron drift may cause anomalous electron transport. However, these 2D PIC simulations are very time-consuming, typically requiring of the order of months to run on multiple processors for a single set of operating conditions.[11,13] Furthermore, reducing the electron density (or equivalently increasing the permittivity of free space) to lower the computational cost appears to directly affect the instability growth rate, amplitude, and hence electron transport.[37] Thus, while 2D or 3D PIC simulations would be ideal to study the electron transport, the large disparity in temporal and spatial scales of the relevant thruster physics makes it difficult to perform detailed parameter studies and test wider ranges of operating conditions. It is therefore of interest to know whether a simpler, faster, 1D reduced simulation model can be developed to more rapidly gain further insight into the electron transport.

Just such a simplified model was recently proposed in Ref. 38, whereby modelling the azimuthal direction, and including a "fake" axial dimension, anomalous electron transport was observed and important new insights were uncovered, such as the strong dependence of the enhanced transport on the electron density. In this paper, we develop an independent 1D PIC simulation to revisit some of these results, and use it to uncover some important additional insights. As a result of these insights, we then develop a kinetic analytical model in Paper II[39] to theoretically explain the anomalous electron transport, from which we are able to propose scaling laws to help model this phenomenon more self-consistently.

II. ELECTRON TRANSPORT ACROSS MAGNETIC FIELDS

Before presenting the PIC simulations, we briefly revise the classical theory of electron transport across a magnetic field. Consider the electron momentum conservation equation,

$$\frac{\partial}{\partial t}(mn_e\mathbf{v}_{de}) + \nabla \cdot (mn_e\mathbf{v}_{de}\mathbf{v}_{de})$$
$$= qn_e(\mathbf{E} + \mathbf{v}_{de} \times \mathbf{B}) - \nabla \cdot \mathbf{\Pi}_e - m\nu_m n_e\mathbf{v}_{de}, \quad (1)$$

where m and q are the electron mass and charge, n_e, $\mathbf{v}_{de}$, and $\mathbf{\Pi}_e$ are the electron density, drift velocity, and pressure tensor; $\mathbf{E}$ and $\mathbf{B}$ are the electric and magnetic fields; and ν_m is the electron-neutral momentum transfer collision frequency. Ignoring the inertial and pressure terms, in the "axial," z, and "azimuthal," y, directions, and assuming a magnetic field in the "radial," x-direction, we can write

$$0 = qn_eE_z - qn_ev_{dey}B_x - m\nu_m n_e v_{dez}, \quad (2)$$

$$0 = qn_eE_y + qn_ev_{dez}B_x - m\nu_m n_e v_{dey}. \quad (3)$$

Since HETs are mechanically azimuthally symmetric, it is usually assumed that there are no gradients in the azimuthal

direction, and so $E_y = 0$. In this case, Eqs. (2) and (3) can be combined to give the classical expression for the cross-field electron mobility,

$$\mu_\perp = \frac{\Gamma_z}{n_eE_z} = \frac{\frac{|q|}{m\nu_m}}{1 + \frac{\omega_{ce}^2}{\nu_m^2}}, \quad (4)$$

where $\Gamma_z = n_ev_{dez}$ is the axial electron flux and $\omega_{ce} = |q|B_x/m$ is the cyclotron frequency. An important property of Eq. (4) is that as $\nu_m \to 0$, we also have that $\mu_\perp \to 0$. Thus, no electron transport occurs when collisions are absent. However, based on extensive work in the literature, as well as the PIC simulation results to be presented below, strong instabilities form in the azimuthal direction which lead to the fluctuations in both the electron density and the azimuthal electric field. If these fluctuations are correlated, then they will not be out-of-phase, and thus averaging over the characteristic instability wavelength and period will yield a non-zero value. In this case, we should instead average Eq. (3) to get

$$0 = q\langle n_eE_y\rangle + q\langle n_ev_{dez}\rangle B_x - m\nu_m\langle n_ev_{dey}\rangle. \quad (5)$$

Then combining this with Eq. (2) (after also averaging), we can obtain a different expression for the cross-field mobility that accounts for the presence of any azimuthal instabilities,

$$\mu_{eff} = \frac{\frac{|q|}{m\nu_m}}{1 + \frac{\omega_{ce}^2}{\nu_m^2}}\left[1 - \frac{\omega_{ce}}{\nu_m}\frac{\langle n_eE_y\rangle}{n_eE_z}\right]. \quad (6)$$

As we will see, $\langle n_eE_y\rangle < 0$, and thus, the effect of azimuthal fluctuations is to enhance the electron mobility. We highlight an important property of Eq. (6): if $\nu_m \to 0$, we now have that $\mu_{eff} \to -\langle n_eE_y\rangle/n_eE_zB$. In general, this term is not equal to zero and, as discussed below, is associated with collective electron-wave scattering due to the azimuthal fluctuations, even in the absence of electron-neutral collisions.

III. DESCRIPTION OF PIC SIMULATIONS

To study the cross-field electron transport, we make use of a simplified PIC simulation (similar to that proposed in Ref. 38), a schematic of which is shown in Figure 1. A uniform "radial" magnetic field, B_0, is applied in the x-direction, and a uniform "axial" electric field, E_0, is applied in the z-direction. The "azimuthal" direction then corresponds to the, $\mathbf{E}_0 \times \mathbf{B}_0$, y-direction. Particle positions are tracked in both the axial and azimuthal directions. The axial electric field component is provided by the spatially and temporally constant applied electric field, E_0, while the azimuthal electric field component is obtained by solving Poisson's equation in the azimuthal direction. In Possion's equation, the charge densities are calculated by weighting all particles to the same 1D azimuthal grid regardless of their axial position. Both electrons and singly charged xenon ions are modelled. Electrons are magnetized and electron-neutral collisions, including single ionization, excitation, and elastic scattering reactions (using cross-sections taken from Ref. 40), are
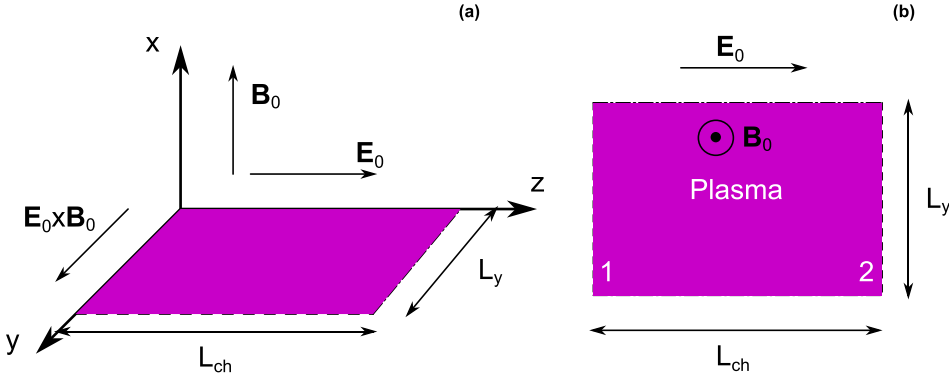
FIG. 1. Schematic of the PIC model showing the (a) relevant field and simulation directions and (b) the y-z simulation plane. A uniform magnetic field, B_0, is applied in the "radial" x-direction, and a uniform electric field, E_0, is applied in the "axial" z-direction. Poisson's equation is then solved in the "azimuthal" y-direction. Particles which cross the axial channel length are replaced with cold particles loaded at the opposite end.

treated using a standard Monte Carlo Collision (MCC) algorithm.[41] The neutral density is assumed uniform with a temperature of 300 K, and pressures between 0 and 1000 mTorr (giving densities between 0 and 3.2×10^{22} m^{-3}) are used in the simulations. During an ionization reaction, only the energy loss and scattering are modelled and new electrons or ions are not added to the simulation. The equations of motion describing ion evolution do not include the magnetic field or ion-neutral collisions.

Periodic boundary conditions are used for Poisson's equation and for the particles at the "azimuthal" boundaries, while a finite axial distance is present to model the ion acceleration region along the thruster channel. Note that while this implies a 2D simulation domain, Poisson's equation is only solved in the "azimuthal" direction on a single 1D mesh irrespective of the particle axial position. Ions that cross the exit plane of the axial region are removed from the simulation and replaced by new ions (with a temperature of $T_i = 0.1$ eV) loaded at the entrance, while electrons that are lost at the entrance plane are removed and replaced with new electrons (with a temperature of $T_e = 2$ eV) loaded at the exit plane. Thus, the total number of particles (and hence average plasma density) remains constant. Particles replaced in this way are loaded with a random azimuthal position. Ions are either allowed to experience the axial electric field or are loaded with a constant axial drift velocity, v_{di}. The effect of the axial electric field on the ion motion is only to change the effective transit time through the acceleration region.

For most of the operating conditions used, simulations reach a steady-state within about 1–2 μs. In the presence of a strong instability, this equilibrium is dynamic, and can show relatively large amplitude oscillations with frequencies in the MHz range. This necessitates long-time averages (of about 10 μs) to obtain relevant transport properties, such as the mobility. Even after this averaging, the mobilities still tend to show a strong variation that can be as much as 20%–30% (which we express as errorbars in the relevant results below). For the simulations, we use between about $N/NG = 100$–1000 particles per cell, with around $NG = 100$–200 grid points (sufficient to more than resolve the Debye length), and time steps of about 5×10^{-12} s to ensure resolution of both the electron plasma frequency, and to satisfy the Courant condition for electrons with energies of up to 280 eV. Unless otherwise stated, Table I lists the standard operating and numerical parameters used in the simulations. These have been chosen to closely resemble those used in the 1D PIC simulations of Ref. 38.

From consideration of the full dispersion relation for a plasma in crossed electric and magnetic fields,[12,39] positive instability growth rates occur for quantized wavenumbers approximately satisfying

$$k_y = \frac{r\omega_{ce}}{v_{de}} \approx \frac{qrB_0^2}{mE_0}, \tag{7}$$

where $k_y = 2\pi/\lambda$ is the "azimuthal" wavenumber, λ is the instability wavelength, r is the mode number, and $v_{de} = E_0/B_0$ is the azimuthal electron drift velocity. For the typical operating conditions used in Table I, and for the first mode ($r = 1$), this gives a wavelength of about 1.8 mm, and thus we have chosen the simulated azimuthal length, L_y, to be larger than this. Within the simulations, the electron cross-field mobility is defined as

$$\mu_{pic} = \frac{\sum_{j=1}^{N} v_{jz}}{NE_0}. \tag{8}$$

Here, the summation is over all electrons in the simulation, and hence $\sum v_{jz}/N$ represents the average axial electron drift velocity.

IV. RESULTS

A. Classical diffusion

Before investigating electron transport under conditions where an instability is present, we confirm that the simulations return the classical mobility relation given by Eq. (4) in the absence of an instability. Instability-enhanced transport

TABLE I. Standard operating and numerical parameters used in the PIC simulations.

Parameter	Value
L_y (cm)	0.5
L_{ch} (cm)	1.0
n_0 (m^{-3})	1×10^{17}
B_0 (G)	200
E_0 (V m^{-1})	2×10^4
v_{di} (ms^{-1})	1×10^4
Δt (s)	5×10^{-12}
NG	100–200
N/NG	100–1000

was effectively turned off by enforcing a near zero azimuthal electric field ($E_y = 0$). This was accomplished by reducing the macroparticle weight of the simulation particles (the electric field is proportional to the plasma density, and hence the macroparticle weight). These results are indicated as $E_y = 0$ in the figures below. By turning off E_y, the instability contribution to the mobility in Eq. (6) is also effectively turned off, leaving the classical relation of Eq. (4). All other simulation parameters correspond to those in Table I. The time-averaged electron cross-field mobility is shown in Figure 2 as a function of the neutral gas pressure. The solid curve shows the mobility from classical theory (Eq. (4)), where the momentum transfer collision frequency, ν_m, has been obtained directly from the simulations by counting the number of collision events per unit time. At high pressures, the mobility is correspondingly high, but decreases as the pressure is reduced. The classical mobility is in good agreement with that found from the simulations, except for very low pressures where a deviation is present. This deviation occurs because the inertial and pressure terms neglected in deriving Eq. (4) can no longer be ignored, and are similar to, or larger than, the collisional momentum loss. If the pressure is set to zero, then the electron mobility is also found to be zero (within statistical limits) in the simulations, as expected from Eq. (4). The results in Figure 2 are in excellent agreement with the corresponding results in Ref. 38.

B. Instability formation and enhanced diffusion

By increasing the plasma density to values similar to those seen near the maximum magnetic field location in HETs, a strong instability is observed to form in the simulations at sufficiently low pressures. The discharge requires about 1–$2\,\mu s$ before the instability saturates and a quasi steady-state is reached, which is characterized by large amplitude fluctuations in the electron and ion densities, electric field, and electron energy. Figure 3 shows contour plots of the spatio-temporal variation of these fluctuations in the (a)

electron density and (b) "azimuthal" electric field for a plasma density of $n_0 = 1 \times 10^{17}\,\mathrm{m^{-3}}$ and a neutral xenon gas pressure of 1 mTorr. The fluctuations in the electron density are around 20%–30% of the equilibrium density, while the amplitude of the electric field fluctuations is larger than the applied "axial" electric field itself. There is also a clearly observed periodic spatial and temporal structure, giving a wavelength of about 1.7 mm and a frequency of about 5 MHz. These values are within the range previously observed in Refs. 11–13, 37, and the wavelength is close to that predicted from Eq. (7). Figure 4 shows the cross-field electron mobility as a function of pressure when an instability is present for $n_0 = 1 \times 10^{17}\,\mathrm{m^{-3}}$. Also shown are the results from Sec. IV A for $E_y = 0$ (zero macroparticle weight), and the mobility from classical theory (Eq. (4)). As seen at high pressures (where no significant instability is present), the mobility is in almost perfect agreement with that for $E_y = 0$ (and hence with classical theory), but as the pressure is reduced, a significant deviation occurs which is as much as one to two orders of magnitude larger than that when $E_y = 0$. Thus, there is an "anomalous" electron transport. Furthermore, the mobility appears to converge to a non-zero asymptotic value. The horizontal dashed line shows the
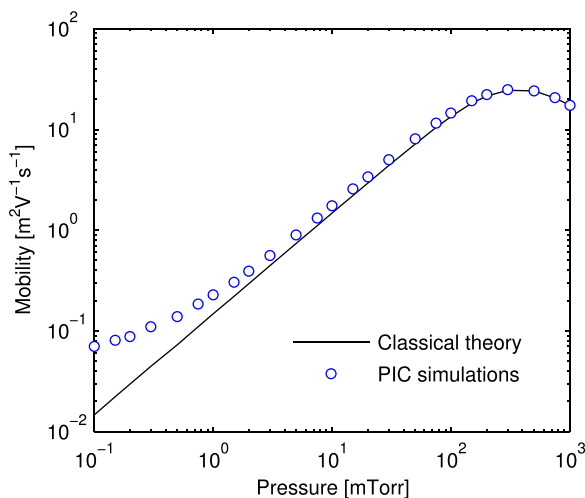

FIG. 2. Cross-field electron mobility as a function of the neutral xenon gas pressure. The solid curve shows the classically expected mobility from Eq. (4). The simulation macroparticle weight is set to near zero for all simulation results to enforce $E_y = 0$.
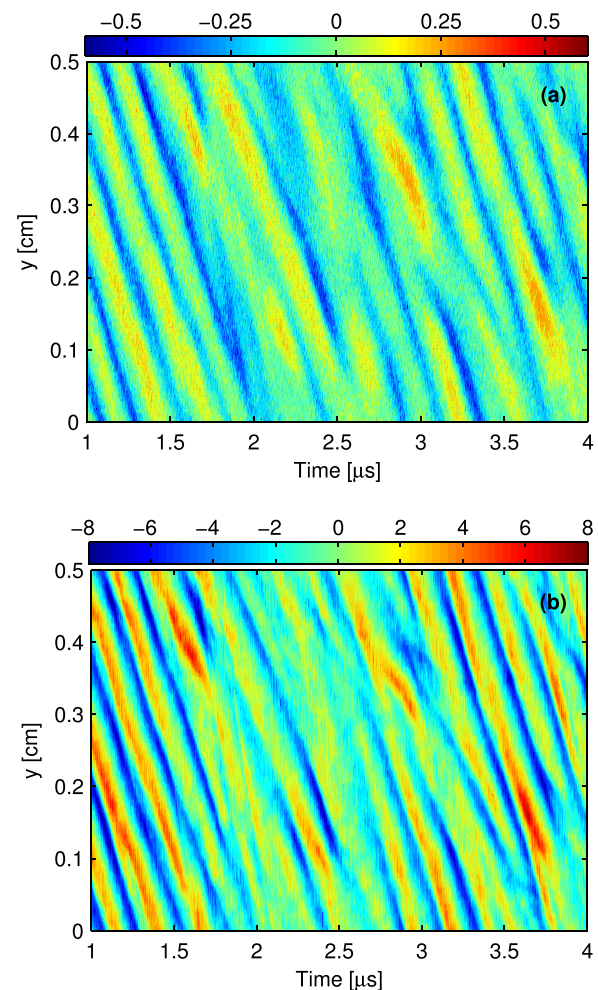

FIG. 3. Contour plots of the spatio-temporal variation of the (a) normalized electron density $(n_e(y, t)/n_0)$ and (b) normalized azimuthal electric field $(E_y(y, t)/E_0)$. The plasma density is $n_0 = 1 \times 10^{17}\,\mathrm{m^{-3}}$ and the neutral xenon pressure is 1 mTorr.
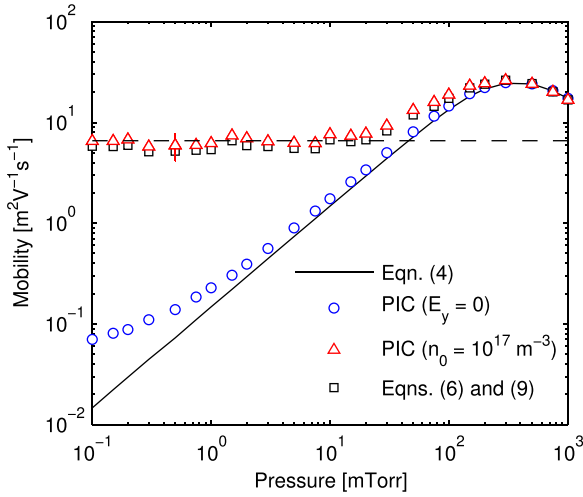
FIG. 4. Cross-field electron mobility as a function of the neutral xenon gas pressure. The blue open circles correspond to simulations with $E_y = 0$ (zero macroparticle weight) and the red open triangles to $n_0 = 1 \times 10^{17} \text{m}^{-3}$. The black open squares are predictions based on Eqs. (9) and (6), while the black solid curve corresponds to classical theory given by Eq. (4).

simulation results if the pressure is set to zero. This establishes an important result: the enhanced electron transport is essentially independent of electron-neutral collisions. This is in contrast to the hypothesis in Ref. 38, but agrees with that first proposed in Ref. 11.

Although difficult to judge by eye, the electron density and electric field fluctuations in Figure 3 are not completely out-of-phase, but are correlated and result in a non-zero value of $\langle n_e E_y \rangle$. This quantity can be calculated from the simulations using

$$\langle n_e E_y \rangle = \int_0^{L_y} \frac{dy}{L_y} \int_0^T \frac{dt}{T} n_e(y,t) E_y(y,t), \tag{9}$$

where the integrals are evaluated numerically by using the electron density and electric field taken from the simulations at each spatial grid location and at each time step, and T is a time period much larger than the characteristic period of the instability. Once $\langle n_e E_y \rangle$ has been calculated from Eq. (9), it can be input into Eq. (6) to determine the electron mobility. These results are shown as the open black squares in Figure 4. As seen, the predicted mobility using this method is in excellent agreement with that found directly from the simulations using Eq. (8) over the entire pressure range simulated. This demonstrates that the "anomalous" mobility is completely described by the correlation term $\langle n_e E_y \rangle$, which represents electron-wave scattering due to the presence of the instability. The very slight difference between the directly computed mobility, and that predicted, is due to neglect of the inertial and pressure terms in the derivation of Eq. (6).

Further evidence of the enhanced electron collisionality due to electron-wave scattering can be found by observing the electron velocity distribution function (EVDF). Figures 5(a) and 5(b) show the time-averaged EVDFs for two simulations, A and B. Case A corresponds to a simulation with $E_y = 0$ (and a pressure of 1 mTorr) and no instability or enhanced transport, while case B corresponds to a simulation with $n_0 = 1 \times 10^{17} \text{m}^{-3}$ (also with a pressure of
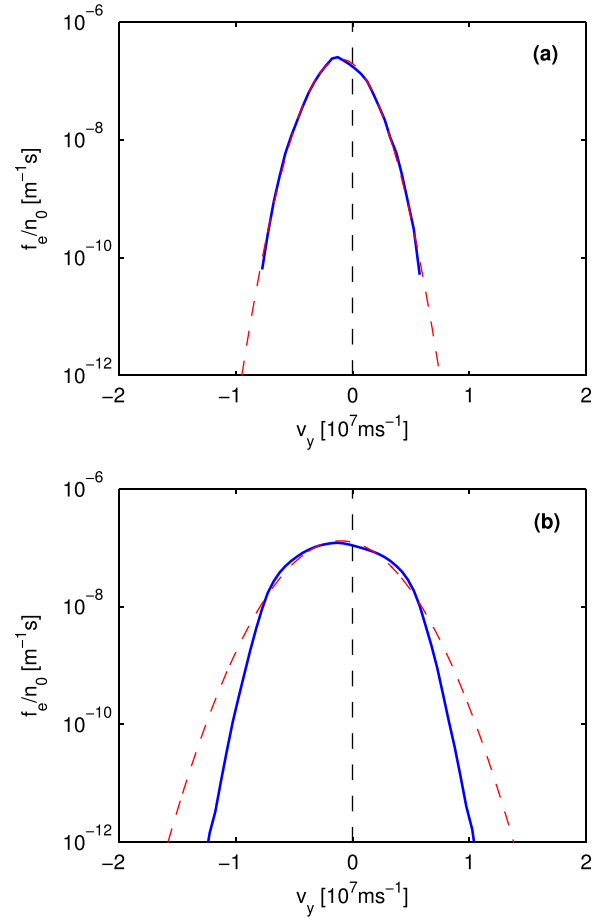

FIG. 5. Electron velocity distribution functions in the "azimuthal" y-direction for (a) $E_y = 0$ (zero macroparticle weight) and (b) $n_0 = 1 \times 10^{17} \text{m}^{-3}$. The neutral xenon gas pressure is zero. The red dashed curves show a drifting Maxwellian distribution given by Eq. (10) with an effective electron temperature found from the simulations.

1 mTorr). Also shown in Figure 5 are Maxwellian EVDFs found from

$$\frac{f_e(v_y)}{n_0} = \frac{1}{\sqrt{\pi} v_{Te}} \exp\left[-\frac{(v_y - v_{de})^2}{v_{Te}^2} \right], \tag{10}$$

where $v_{de} = E_0/B_0$, and $v_{Te} = \sqrt{2qT_e/m}$ with $T_e = 2\langle \varepsilon_y \rangle$ (and in units of [eV]) and with $\langle \varepsilon_y \rangle$ the time-averaged electron energy in the y-direction. The EVDF in Figure 5(a) is in excellent agreement with the Maxwellian from Eq. (10), whereas the EVDF in Figure 5(b) is clearly different and shows a much flatter gradient for velocities close to v_{de}, and a much faster drop off at higher velocities. This distortion of the EVDF is similar to that observed previously in Refs. 11 and 12 and is characteristic of velocity-space diffusion due to enhanced collisionality.[43]

C. Effect of statistical noise

Because of the statistical nature of PIC simulations, it is important to ascertain the dependence or sensitivity of the results on the number of particles used, particularly since we showed in Sec. IV B that the enhanced electron transport does not require electron-neutral collisions. Figure 6 shows the
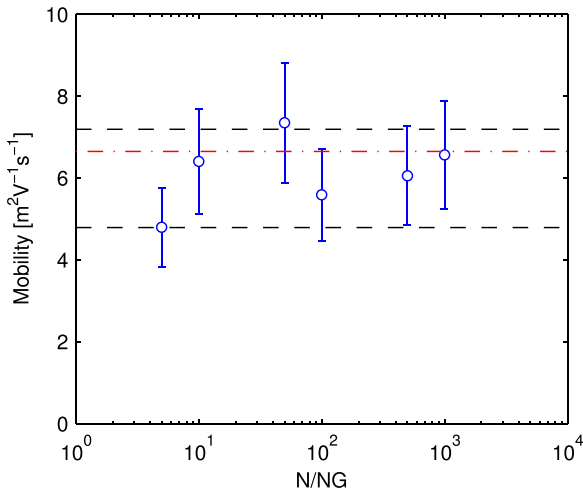
FIG. 6. Cross-field electron mobility as a function of the number of particles per cell. The data points correspond to $NG = 200$, while the horizontal dashed lines are the upper and lower bounds for a simulation with $NG = 100$ and $N/NG = 100$. The neutral xenon gas pressure is zero. The red dotted line shows the results when particles are loaded using a "quiet start" algorithm (see Sec. IV C).

cross-field electron mobility as a function of the number of particles per cell (N/NG). The values of N/NG chosen span the typical range used in most previous PIC simulations.[11,13,37] The neutral xenon gas pressure is set to zero, and the simulation parameters are the same as those in Table I. The data points correspond to 200 grid points, while the horizontal dashed lines mark the upper and lower bounds for a simulation with $NG = 100$ and $N/NG = 100$. As seen, while there is some scatter in the results, they are all close to the average mobility of $6\,\mathrm{m}^2\mathrm{V}^{-1}\mathrm{s}^{-1}$. Furthermore, increasing the number of particles per cell does not appear to reduce the scatter.

As has been known since some of the earliest PIC simulations,[42] the initial loading of particles in the simulation domain can result in density and electric field fluctuation levels that are already fully developed and significantly higher than those of an initially stable plasma. In the present simulations, we have loaded particles randomly in phase space, as demonstrated in Figure 7(a), which shows a plot of the electron velocities perpendicular to the magnetic field. In order to check that initial fluctuation levels due to particle loading are not responsible for the enhanced transport, we have also performed tests where particles are loaded using a "quiet start" algorithm based on binary and trinary bit-reversed numbers (as discussed in Ref. 42), leading to the more ordered phase space in Figure 7(b). For these simulations, the initial fluctuation level is much lower, but eventually, rapidly increases as the instability forms, leading to behaviour identical to that seen with the standard random particle loading. The red dotted line in Figure 6 shows the time-averaged mobility for this case, where similar results are found. Thus, the results do not appear to be sensitive to the numerical simulation parameters or particle loading conditions, indicating that the instability, and associated enhanced transport, is quite a robust phenomenon.

D. Instability saturation

In almost all of the simulations above, we have used a finite axial channel length, removing particles that cross the
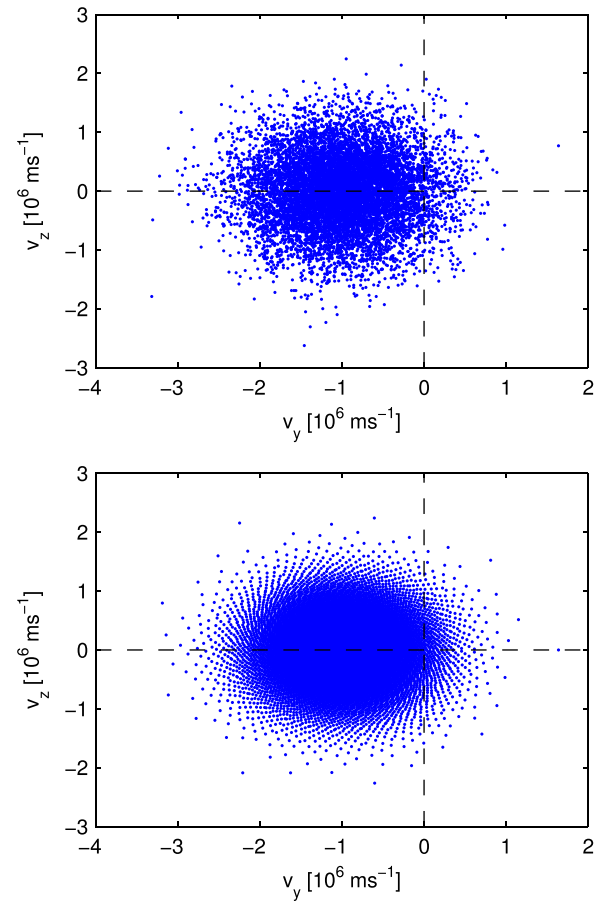

FIG. 7. Electron velocity phase space perpendicular to the magnetic field obtained using (a) random numbers with a normal distribution and (b) a "quiet start" algorithm based on bit-reversed numbers.

boundaries of this region. These axial boundary conditions were found to be needed in order to observe saturation of the instability. Figure 8 shows the average electron energy as a function of time for the standard operating conditions with the axial boundary conditions imposed (blue solid line), and also with the axial boundary conditions removed (red dashed
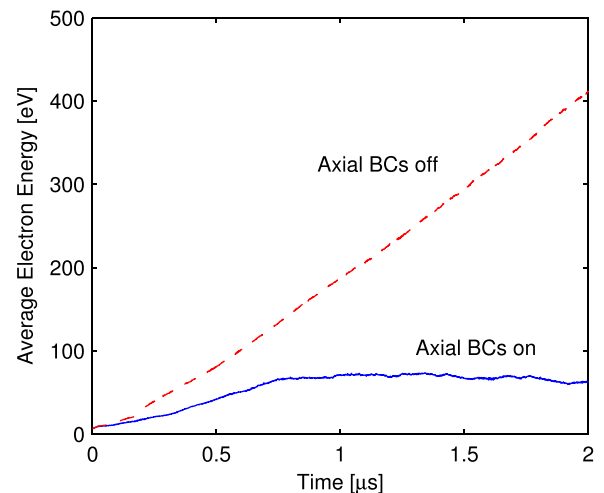

FIG. 8. Average electron energy as a function of time for a simulation with (a) "axial" boundary conditions imposed and (b) "axial" boundary conditions removed. The plasma density is $n_0 = 1 \times 10^{17}\,\mathrm{m}^{-3}$ and the neutral xenon pressure is zero.

line). This latter case is achieved by using an infinitely long axial channel so that particles never reach the boundaries but rather can proceed indefinitely in the axial direction. Note that since Poisson's equation is only solved in the azimuthal direction, there is no grid needed in the axial direction. As seen, when the boundary conditions are imposed a quasi-equilibrium is reached after about 1–2 μs, and the average electron energy has increased to about 65 eV (giving an effective temperature of about 43 eV), while if the boundary conditions are not imposed, the electron energy continues to increase, and after 2 μs is close to 400 eV (giving an effective temperature of around 260 eV). These latter energies/temperatures are almost 10 times higher than those seen experimentally, and indicate that for instability saturation the electron distribution must distort to reduce the growth rate (as also previously observed in Ref. 12).

Usually, after a few growth times (1/γ where γ is the instability growth rate), nonlinear effects begin to dominate the subsequent evolution of an instability and limit further growth. In this case, saturation often occurs due to particle-wave trapping.[44] Observation of the electron and ion phase space plots shows no obvious signs of electron trapping, but definite evidence of ion trapping, as clearly demonstrated in Figure 9, where the axial boundary conditions have been used. This ion trapping behaviour was observed in virtually all simulations where an instability formed, and indicates that the trapping phenomenon likely plays a key role in limiting further growth of the instability amplitude. Indeed, the amplitude of the fluctuations in the plasma potential, $\delta\phi$, for the simulation in Figure 9 is about 40–50 V, while the ion energy, ε_i, at the phase velocity of the instability (found from $v_{phase} = f\lambda$ where $f \sim 5$ MHz and $\lambda \sim 1.7$ mm) is about 50 eV, thus we have

$$\delta\phi \approx \frac{1}{2}\frac{M}{q}v_{phase}^2. \tag{11}$$

Figure 10 shows a plot of the amplitude of fluctuations in the plasma potential, and the ion energy at the phase velocity for
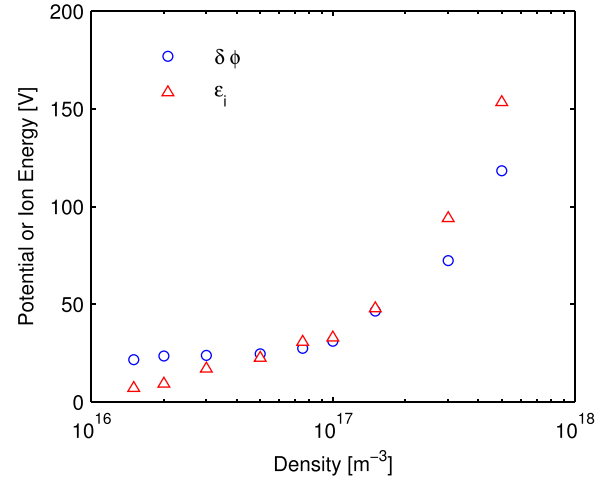
FIG. 10. Amplitude of the fluctuations in the potential, $\delta\phi$, and the ion energy at the instability phase velocity, ε_i, as a function of plasma density. The neutral xenon gas pressure is zero.

simulations with different plasma densities. In some of the simulations, it is difficult to estimate an accurate phase velocity because the instabilities are composed of multiple frequencies/wavenumbers. Nevertheless, trapping in the ion phase space is seen in all cases, and the correlation of the potential and the energy in Figure 10 is quite close, providing further evidence supporting Eq. (11). From the theory of beam-cyclotron instabilities,[45,46] after a few growth times, nonlinear turbulent effects set in which act to "smear" out the quantized nature of the plasma dispersion relation, causing a transition to an ion-acoustic type instability (which leads to a linear dispersion relation, which has also been observed experimentally in HETs[47]). After further growth, this ion-acoustic instability then saturates due to ion-wave trapping. This view is consistent with that observed in the simulations here. Thus, while convection out of the simulation region was needed for saturation (as seen in Fig. 8), this appears to occur together with ion-wave trapping. The combination of these points will prove instrumental in establishing a theoretical model to describe the anomalous electron transport as discussed in Paper II,[39] where ion-wave trapping determines the electric field and electron density fluctuation amplitudes, while convection determines the instability growth rate (and hence phase shift between the electric field and density fluctuations) at saturation.

E. Axial boundary conditions

In most of the simulation results in Secs. IV A–IV D, we have made use of a finite thruster channel length, and removed particles that cross the axial boundaries while loading new particles at the opposite boundaries. In order to confirm that this does not create an artifact which causes the enhanced electron transport, a set of test simulations was run with the axial boundary conditions removed. This was again achieved by using an infinitely long axial channel so that particles never reach the axial boundaries. Figure 11 shows the "axial" and "azimuthal" positions of simulation electrons after 1 μs for 2 cases: (a) $E_y = 0$ and a pressure of zero, and (b) $n_0 = 1 \times 10^{17}$ m^{-3} and also with a pressure of zero. For
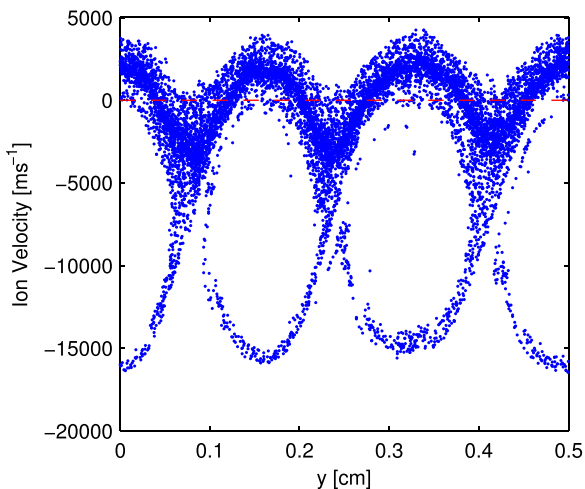

FIG. 9. Ion phase space in the "azimuthal" direction showing the characteristic "loops" indicative of trapping in an electrostatic wave. The plasma density is $n_0 = 1 \times 10^{17}$ m^{-3} and the neutral xenon pressure is zero.
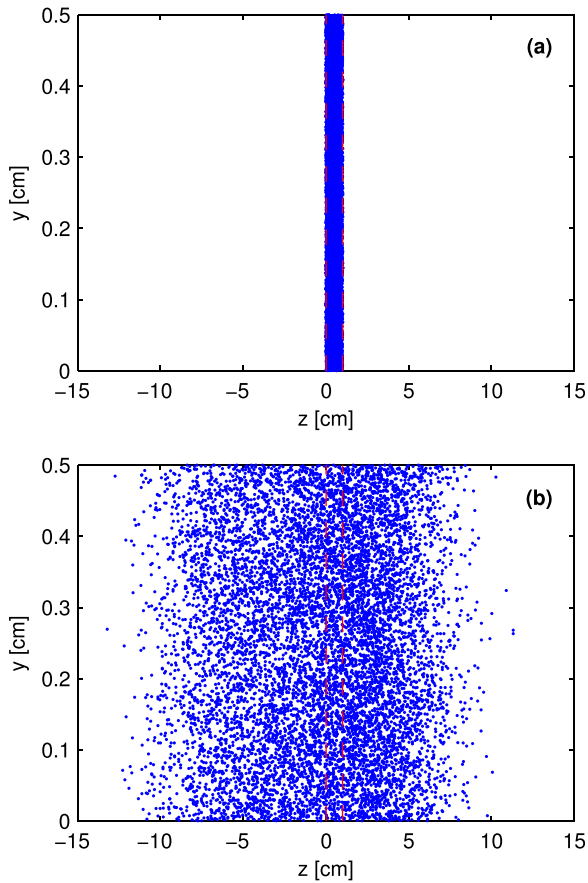
FIG. 11. "Axial" and "azimuthal" locations of simulation electrons after 1 μs for (a) $E_y = 0$ (zero macroparticle weight) and a pressure of zero and (b) $n_0 = 1 \times 10^{17} \mathrm{m}^{-3}$ and a pressure of zero. The red vertical dashed lines indicate the initial simulation region where electrons were loaded.

case (a), there is no instability present, and since there are no collisions, electrons cannot diffuse axially and so remain confined in the initial loading region. For case (b), however, even though there are no explicit electron-neutral collisions, clear evidence of axial electron diffusion can be seen. Some electrons are also seen to move to the right depending on where in their gyro-orbit they suffer a collision, but more electrons still drift to the left because of the sign of the applied axial electric field. If this axial electric field is reversed, then the above behaviour is also reversed.

The unstable modes that are allowed to develop in the simulations are set by the "azimuthal" simulation length, L_y. However, because of turbulent effects and distortion of the EVDF, the unstable modes can vary significantly in time. For some conditions, it was found that after a simulation had appeared to reach equilibrium, a transition would be observed and the wavelength and/or frequency of the instability would change. Similar behaviour has been observed previously in Ref. 12. This behaviour also appears to be strongly related to the presence of a finite channel and the associated axial boundary conditions. Because Poisson's equation is not solved in the axial direction in the PIC simulations (it is only solved in the azimuthal direction), the wavenumber in this direction is zero, and hence so to is the wave group velocity and any wave convection. The removal of particles that cross the axial boundaries acts as a type of

convection mechanism, but does not correctly capture the true physics.

The above can be easily demonstrated by running simulations with different "azimuthal" lengths and turning the axial boundary conditions on or off. Figure 12 shows the spatio-temporal electric field for "azimuthal" lengths of 0.5 cm and 1 cm, respectively, when the axial boundary conditions are not enforced (all other conditions correspond to those in Table I). In this case, the simulation represents an infinite plasma where there is no wave convection, only growth in time. Since the dominant wavenumber/wavelength is given by Eq. (7), by doubling the periodic length, we expect to observe an identical behaviour but to see twice as many wavelengths in the simulation domain. As seen in Figure 12, after a short time a clear monochromatic travelling wave is observed, which shows 3 wavelengths in the "azimuthal" direction for $L_y = 0.5$ cm, and 6 wavelengths for $L_y = 1$ cm. The instability behaviour is otherwise identical as expected.

By contrast, if the axial boundary conditions are activated, and if the "azimuthal" simulation length is doubled, we observe a completely different behaviour, as demonstrated in Figure 13. Whereas a travelling wave develops for $L_y = 0.5$ cm showing 3 wavelengths (similar to that in Fig. 12), for $L_y = 1$ cm a completely different behaviour is observed with a transition to a single wavelength equal to the length of the entire simulation domain. Similar results were observed for certain combinations of operating parameters.
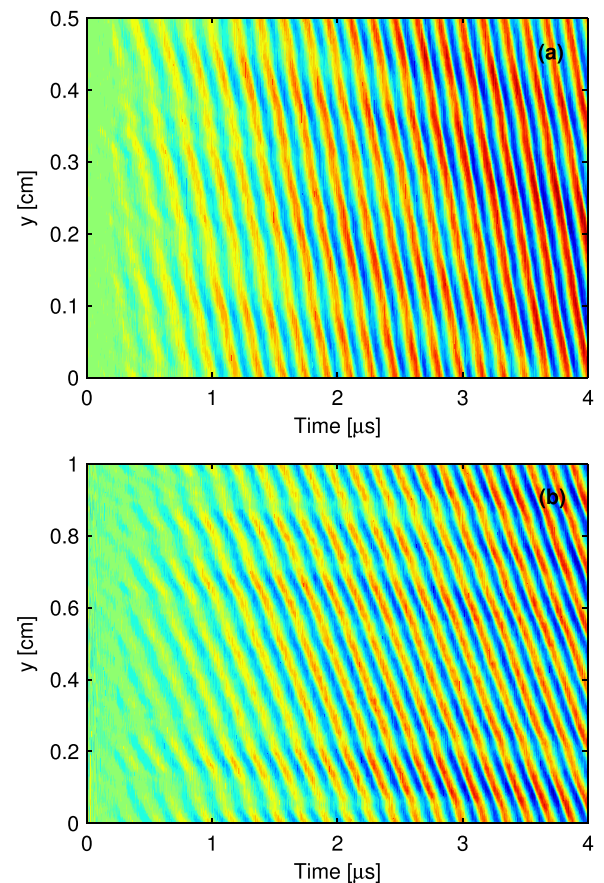

FIG. 12. Spatio-temporal electric field with the axial boundary conditions removed for (a) $L_y = 0.5$ cm and (b) $L_y = 1$ cm. The neutral xenon gas pressure is zero, and all other parameters are the same as those in Table I.
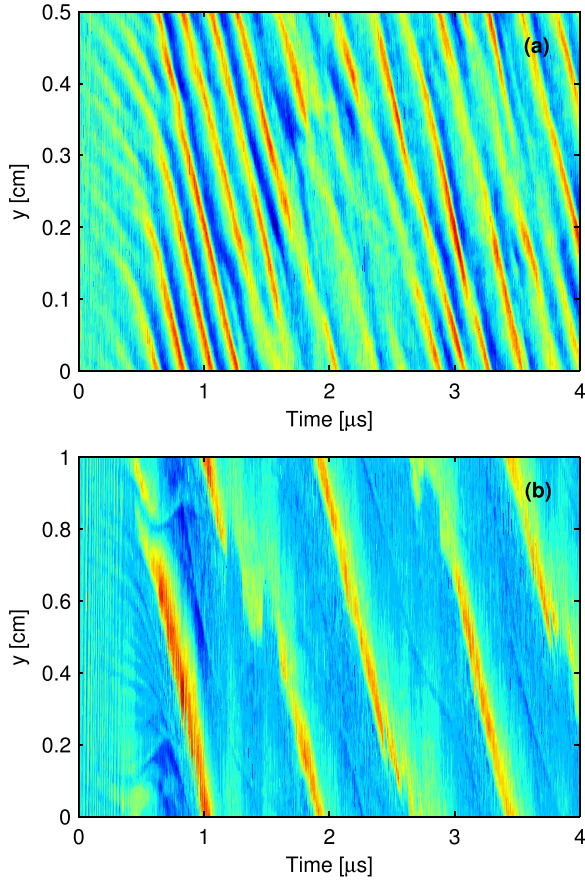
FIG. 13. Spatio-temporal electric field with the axial boundary conditions activated for (a) $L_y = 0.5$ cm and (b) $L_y = 1$ cm. The neutral xenon gas pressure is zero and all other parameters are the same as those in Table I.

Since this behaviour is completely counterintuitive, and is not consistent with the results in Figure 12, when the axial BCs removed, we believe it is an artifact of the 1D model related to the unphysical instability convection that cannot be adequately modelled in 1D.

F. Parametric study

In Secs. IV A–IV E, we have shown that a strong azimuthal instability forms that leads to enhanced electron transport. Here, we vary some of the standard operating parameters in Table I to show that this enhanced transport occurs over a broader parameter space than that used above.
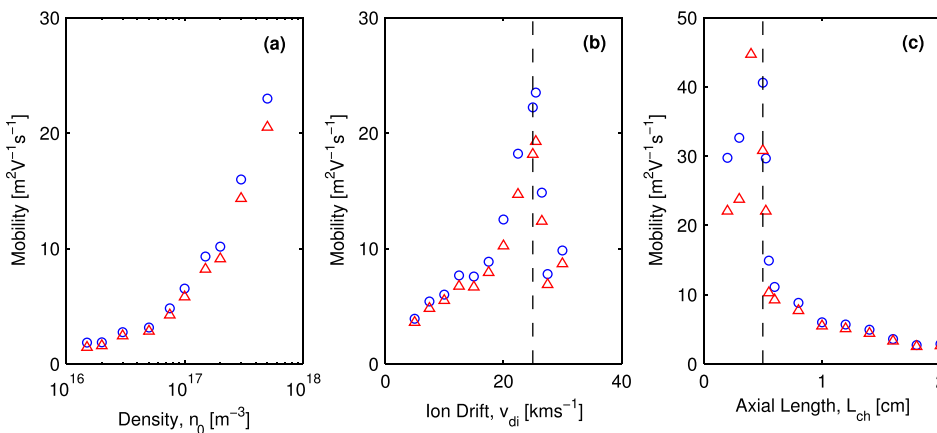
In Figure 14, we plot the cross-field electron transport as a function of (a) plasma density, (b) ion drift velocity, and (c) "axial" thruster length. The open circles show the mobility found from Eq. (8), while the open triangles show the mobility from Eqs. (6) and (9). The plasma density is seen to significantly affect the mobility, which can be expected because the instability growth rate[12,39] and the saturated electric field fluctuation amplitude[39] increase with an increasing density. This strong dependence with the plasma density agrees with the independent PIC simulations in Ref. 38. Similarly, the mobility increases with increasing ion velocity until a certain point, while it decreases with increasing axial length. In Paper II,[39] we present a kinetic theory to predict the anomalous electron transport where the correlation term (and hence mobility in the limit of zero electron-neutral collisions) is found to be proportional to $d(v_{di} n_e T_e)/dz$. Applying this to the axial direction of the present simulations, and noting that ions enter the domain with close to zero drift and using $dz \approx \Delta z = L_{ch}$, we have $\mu_{eff} \propto v_{di}/L_{ch}$. This dependence, due to instability convection,[39] seems consistent with the results in Figure 14. For simulations to the right of the dashed line in Figure 14(b) and the left of the dashed line in (c), the instability wavelength undergoes a dramatic change, possibly indicating a mode jump.

In almost all cases, the mobility in Figure 14 calculated from Eq. (8) and Eqs. (6) and (9) agrees very well. Although we have found the correlation term $\langle n_e E_y \rangle$ in Eq. (6) from the PIC simulations, the fact that the two different mobility calculation methods agree so well indicates that it is indeed this correlation term that is responsible for the anomalous transport. As a result of this insight, in Paper II,[39] we develop a kinetic theory to explicitly predict this term.

V. DISCUSSION AND CONCLUSIONS

In Sec. IV, we have presented the results from a simplified PIC simulation where enhanced electron cross-field transport has been observed. This enhanced transport is associated with the formation of a strong instability in the azimuthal direction, leading to correlated fluctuations in both the electron density and the electric field. The instability is a strong function of the plasma density and can lead to an effective cross-field mobility many orders of magnitude larger than that expected from classical electron-neutral

FIG. 14. Cross-field electron mobility as a function of (a) plasma density, (b) ion drift velocity, and (c) "axial" thruster length. The open circles show the mobility found directly from Eq. (8), while the open triangles show the predicted mobility from Eqs. (6) and (9). The neutral xenon gas pressure is zero for all simulations. For simulations to the right of the vertical dashed line in (b), or left of the line in (c), the instability wavelength is observed to significantly differ.

collisions. Electron scattering off of these collective instability fluctuations acts as an important additional momentum loss mechanism that plays a similar role to standard collisions. Although this momentum loss is in the azimuthal direction, the presence of the magnetic field effectively couples this loss into the axial (cross-field) direction. Furthermore, this process is independent of electron-neutral collisions (in the pressure range relevant to HETs), as well as electron-wall collisions and secondary electron emission (which were not included in the model). A modified formula for the enhanced mobility has been proposed and shown to be in excellent agreement with the results. This formula depends on an electron density-electric field correlation term which we have calculated from the simulations. In Paper II,[39] we extend the present work by explicitly developing a theoretical model to describe this correlation term, thus removing the need for any simulation input.

A number of studies have suggested that electron wall collisions and secondary electron emission could be important in the electron cross-field transport.[3,8,9,18] However, since enhanced transport has been observed both in the results above, as well as the more detailed 2D PIC simulations in Refs. 11 and 37 (neither of which include secondary electrons in the model), this suggests that wall effects probably play an auxiliary role. Any changes in thruster wall materials in a real device would naturally be expected to modify the electron distribution function, and hence the ionization and plasma density profiles. But as demonstrated above, because the instability is a strong function of the plasma density, these changes will naturally affect the electron transport. The important point though is that the azimuthal drift instability is still the primary cause of this enhanced transport. Because our focus in the present work has been to more clearly understand the basic physics in the azimuthal direction of an HET, we have used a simplified simulation model, and it is thus important to briefly discuss some of the limitations of this approach. Although we have not self-consistently modelled some important, more obvious pieces of physics such as the plasma generation, the major shortcomings of the simulation are: (1) all particles, regardless of radial or axial position, are weighted to the same azimuthal grid and (2) since Poisson's equation is only solved in the azimuthal direction, the radial and axial wavenumbers of any fluctuations are necessarily zero. Point (1) implies that there could be an artificial correlation established between the particle motions and the azimuthal electric field, while point (2) implies that convection of the instability (due to a finite group velocity) away from the simulation region is not correctly modelled. The latter point is particularly important, since it was explicitly demonstrated that varying the acceleration length and/or ion drift velocity has a significant effect on the electron transport, and that a steady state solution is only obtained if particle loss from the boundaries is included. The impact of both of the above points is that the level of electron transport in the simulations is mostly likely exaggerated compared with that in 2D simulations and in a real thruster. Indeed, for similar operating conditions to typical HETs, the mobility from the simulations here is about one order of magnitude (or more) higher than that seen

experimentally.[5] Nevertheless, useful insight has been gained from these simplified simulations, which will prove to be of paramount importance in the development of a theoretical model to describe the enhanced transport as discussed in Paper II.[39]

ACKNOWLEDGMENTS

[1]A. I. Morozov and V. V. Savelyev, in *Reviews of Plasma Physics*, edited by B. B. Kadomtsev and V. D. Shafranov (Springer Science+Business Media, New York, 2000).

[2]V. V. Zhurin, H. R. Kaufman, and R. S. Robinson, Plasma Sources Sci. Technol. **8**, R1 (1999).

[3]D. M. Goebel and I. Katz, *Fundamentals of Electric Propulsion: Ion and Hall Thrusters* (Wiley, New Jersey, 2008).

[4]N. B. Meezan, W. A. Hargus, Jr., and M. A. Cappelli, Phys. Rev. E **63**, 026410 (2001).

[5]J. C. Adam, J. P. Boeuf, N. Dubuit, M. Dudeck, L. Garrigues, D. Gresillon, A. Heron, G. J. M. Hagelaar, V. Kulaev, N. Lemoine, S. Mazouffre, J. Perez Luna, V. Pisarev, and S. Tsikata, Plasma Phys. Controlled Fusion **50**, 124041 (2008).

[6]L. Garrigues, J. Pérez-Luna, J. Lo, G. J. M. Hagelaar, J. P. Boeuf, and S. Mazouffre, Appl. Phys. Lett. **95**, 141501 (2009).

[7]I. Katz, I. G. Mikellides, B. A. Jorns, and A. L. Ortega, in Joint Conference of 30th International Symposium on Space Technology and Science 34th International Electric Propulsion Conference and 6th Nanosatellite Symposium, IEPC-2015-402 (The Electric Rocket Propulsion Society, Hyogo-Kobe, Japan, 2015).

[8]I. D. Kaganovich, Y. Raitses, D. Sydorenko, and A. Smolyakov, Phys. Plasmas **14**, 057104 (2007).

[9]D. Sydorenko, A. Smolyakov, I. Kaganovich, and Y. Raitses, Phys. Plasmas **15**, 053506 (2008).

[10]M. Hirakawa, in 25th International Electric Propulsion Conference, IEPC-97-021 (The Electric Rocket Propulsion Society, Worthington, OH, 1997).

[11]J. C. Adam, A. Héron, and G. Laval, Phys. Plasmas **11**, 295 (2004).

[12]A. Ducrocq, J. C. Adam, A. Héron, and G. Laval, Phys. Plasmas **13**, 102111 (2006).

[13]A. Héron and J. C. Adam, Phys. Plasmas **20**, 082313 (2013).

[14]F. Taccogna, S. Longo, M. Capitelli, and R. Schneider, Appl. Phys. Lett. **94**, 251502 (2009).

[15]A. Morozov, Y. Esipchuk, A. Kapulkin, V. Nevrovskii, and V. Smirnov, Sov. Phys. - Tech. Phys. **17**, 482 (1972).

[16]D. Escobar and E. Ahedo, Phys. Plasmas **21**, 043505 (2014).

[17]W. Frias, A. I. Smolyakov, I. D. Kaganovich, and Y. Raitses, Phys. Plasmas **19**, 072112 (2012); **20**, 052108 (2013).

[18]N. Gascon, M. Dudeck, and S. Barral, Phys. Plasmas **10**, 4123 (2003).

[19]C. Boniface, L. Garrigues, G. J. M. Hagelaar, and J. P. Boeuf, Appl. Phys. Lett. **89**, 161503 (2006).

[20]G. J. M. Hagelaar, J. Bareilles, L. Garrigues, and J. P. Boeuf, J. Appl. Phys. **93**, 67 (2003).

[21]N. B. Meezan and M. A. Cappelli, Phys. Rev. E **66**, 036401 (2002).

[22]F. I. Parra, E. Ahedo, J. M. Fife, and M. Martínez-Sánchez, J. Appl. Phys. **100**, 023304 (2006).

[23]A. N. Smirnov, Y. Raitses, and N. J. Fisch, IEEE Trans. Plasma Sci. **34**, 132 (2006).

[24]S. Yoshikawa and D. J. Rose, Phys. Fluids **5**, 334 (1962).

[25]G. S. Janes and R. S. Lowder, Phys. Fluids **9**, 1115 (1966).

[26]E. Y. Choueiri, Phys. Plasmas **8**, 1411 (2001).

[27]A. W. Smith and M. A. Cappelli, Phys. Plasmas **16**, 073504 (2009).

[28]M. K. Scharfe, N. Gascon, M. A. Cappelli, and E. Fernandez, Phys. Plasmas **13**, 083505 (2006).

[29]J. Cavalier, N. Lemoine, G. Bonhomme, S. Tsikata, C. Honoré, and D. Grésillon, Phys. Plasmas **20**, 082107 (2013).

[30]J. P. Boeuf and L. Garrigues, J. Appl. Phys. **84**, 3541 (1998).

[31] J. Bareilles, G. J. M. Hagelaar, L. Garrigues, C. Boniface, J. P. Boeuf, and N. Gascon, Phys. Plasmas 11, 3035 (2004).

[32] I. G. Mikellides, I. Katz, and R. R. Hofer, in 47th AIAA/ASME/SAE/ASEE Joint Propulsion Conference & Exhibit, AIAA-2011-5809 (American Institute of Aeronautics and Astronautics, San Diego, CA, 2011).

[33] R. R. Hofer, I. G. Mikellides, I. Katz, and D. M. Goebel, in 43rd AIAA/ASME/SAE/ASEE Joint Propulsion Conference & Exhibit, AIAA-2007-5267 (American Institute of Aeronautics and Astronautics, Cincinnati, OH, 2007).

[34] M. Keidar, I. D. Boyd, and I. I. Beilis, Phys. Plasmas 8, 5315 (2001).

[35] J. J. Sazbo, "Fully kinetic modeling of a plasma thruster," Ph.D. thesis, Massachusetts Institute of Technology, 2001.

[36] J. W. Koo and I. D. Boyd, Phys. Plasmas 13, 033501 (2006).

[37] P. Coche and L. Garrigues, Phys. Plasmas 21, 023503 (2014).

[38] J. P. Boeuf, Front. Phys. 2, 74 (2014).

[39] T. Lafleur, S. D. Baalrud, and P. Chabert, "Theory for the anomalous electron transport in Hall effect thrusters. II. Kinetic model," Phys. Plasmas 23, 053503 (2016).

[40] A. V. Phelps, see http://jila.colorado.edu/~avp/collision_data/electronneutral/ELECTRON.TXT for compilation of atomic and molecular data, 2005.

[41] V. Vahedi and M. Surendra, Comput. Phys. Commun. 87, 179 (1995).

[42] C. K. Birdsall and A. B. Langdon, Plasma Physics via Computer Simulation (McGraw-Hill, New York, 1985).

[43] R. C. Davidson, Methods in Nonlinear Plasma Theory (Academic Press, New York, 1972).

[44] R. L. Dewar, Phys. Fluids 16, 431 (1973).

[45] M. Lampe, W. M. Manheimer, J. B. McBride, J. H. Orens, K. Papadopoulos, R. Shanny, and R. N. Sudan, Phys. Fluids 15, 662 (1972).

[46] M. Lampe, W. M. Manheimer, J. B. McBride, J. H. Orens, R. Shanny, and R. N. Sudan, Phys. Rev. Lett. 26, 1221 (1971).

[47] S. Tsikata, N. Lemoine, V. Pisarev, and D. M. Grésillon, Phys. Plasmas 16, 033506 (2009).